WPJET2-PR(18) 20967

P Stroem et al.

Analysis of deposited layers with deuterium and impurity elements on samples from the divertor of JET with ITER-like wall

Preprint of Paper to be submitted for publication in
Journal of Nuclear Materials

This work has been carried out within the framework of the EUROfusion Consortium and has received funding from the Euratom research and training programme 2014-2018 under grant agreement No 633053. The views and opinions expressed herein do not necessarily reflect those of the European Commission.

Analysis of deposited layers with deuterium and impurity elements on samples from the divertor of JET with ITER-like wall

P. Ström[a*], P. Petersson[a], M. Rubel[a], E. Fortuna-Zaleśna[b], A. Widdowson[c], G. Sergienko[d] and JET Contributors[**]

EUROfusion Consortium, JET, Culham Science Centre, OX14 3DB, Abingdon, UK
[a]Department of Fusion Plasma Physics, Royal Institute of Technology (KTH), 10044 Stockholm, Sweden
[b]Warsaw University of Technology, 02-507 Warsaw, Poland
[c]Culham Centre for Fusion Energy, Culham Science Centre, Abingdon, OX14 3DB, UK
[d]Forschungszentrum Jülich GmbH, Institut für Energie- und Klimaforschung – Plasmaphysik, 52425 Jülich, Germany

*Corresponding author
email: pestro@kth.se
Postal address: KTH, Fusion Plasma Physics,
Teknikringen 31, 114 28, Stockholm

Abstract

Inconel-600 blocks and stainless steel covers for quartz microbalance crystals from remote corners in the JET-ILW divertor were studied with time-of-flight elastic recoil detection analysis and nuclear reaction analysis to obtain information about the areal densities and depth profiles of elements present in deposited material layers. Surface morphology and the composition of dust particles were examined with scanning electron microscopy and energy-dispersive X-ray spectroscopy. The analyzed components were present in JET during three ITER-like wall campaigns between 2010 and 2017. Deposited layers had a stratified structure, primarily made up of beryllium, carbon and oxygen with varying atomic fractions of deuterium, up to more than 20%. The range of carbon transport from the ribs of the divertor carrier was limited to a few centimeters, and carbon/deuterium co-deposition was indicated on the Inconel blocks. High atomic fractions of deuterium were also found in almost carbon-free layers on the quartz microbalance covers. Layer thicknesses up to more than 1 micrometer were indicated, but typical values were on the order of a few hundred nanometers. Chromium, iron and nickel fractions were less than or around 1% at layer surfaces while increasing close to the layer-substrate interface. The tungsten fraction depended on the proximity of the plasma strike point to the divertor corners. Particles of tungsten, molybdenum and copper with sizes less than or around 1 micrometer were found. Nitrogen, argon and neon were present after plasma edge cooling and disruption mitigation. Oxygen-18 was found on component surfaces after injection, indicating in-vessel oxidation. Compensation of elastic recoil detection data for detection efficiency and ion-induced release of deuterium during the measurement gave quantitative agreement with nuclear reaction analysis, which strengthens the validity of the results.

Keywords: Fusion, Tokamak, Plasma-wall interactions, ToF-ERDA, NRA, SEM

[**]See the author list of X. Litaudon et al., Nucl. Fusion 57 (2017) 102001.

1. Introduction

Plasma-wall interactions, material migration and the resulting surface modification of plasma facing components are identified as key elements in the preparation for future fusion devices [1]. To facilitate material migration studies in the Joint European Torus (JET) with ITER-like wall [2,3], a significant number of probes have been installed; both in the divertor and in the main chamber [4]. Such probes are retrieved for ex-situ analysis during major shutdowns. The aim of this paper is to provide an analysis of deposited layers on components retrieved from remote corners in the JET divertor between 2012 and 2017, after three ITER-like wall campaigns (ILW-1 to ILW-3). Layer thickness, composition and depth profiles of atomic concentrations are investigated. Conclusions about material deposition are drawn while keeping in mind uncertainties and error sources related to the chosen analysis methods. Sample surface morphology and the presence of dust particles are also described. The analysed components are cubic blocks of Inconel-600 with side length 15 mm, referred to as spatial blocks (SB) and 76 mm long stainless steel covers for quartz microbalance (QMB) deposition monitors.

2. Experimental

2.1 Sample descriptions and plasma exposure conditions

Five SB were included in the present study; SB 4, 5, 6, 8 and 9, all of which, while present in JET, were attached to the carbon ribs of the divertor carrier in Module 14 inner wide (IW) beneath and behind Tile 3. SB4-6 were in the machine between 2011 and 2012, during ILW-1 while SB8-9 were present from 2015 to 2016, during ILW-3. Two sets of four QMB covers each, numbered 1, 2, 3 and 5 were studied. The first such set was present in JET between 2012 and 2014, during ILW-2, except the cover for QMB1 which was present from 2010 to 2014, during ILW-1-2. The second set was present during ILW-3 and removed from JET in 2017. QMB1 was located on the divertor carrier in Module 13 IW behind Tile 3. QMB2 and QMB3 were similarly positioned but in Module 2 IW. QMB5 was located in Module 2 outer wide (OW) behind Tile 7 [5, 6]. Full descriptions of the divertor geometry with the locations of the QMBs and tiles mentioned here can be found in Ref. [3] and [7]. Module numbers refer to a toroidal partitioning of JET into 24 sections, each covering 15°. A difference in module numbers therefore corresponds to approximately 15 times that difference in toroidal angle between the positions of the components. The total divertor plasma times in JET with cutoff at plasma current 100 kA for campaigns ILW-1, 2 and 3 were approximately 45 000 s, 50 000 s and 67 000 s, with total energy input 150, 201 and 245 GJ respectively. Limiter plasma times were 27 000 s, 22 000 s and 18 000 s. The most common plasma species was D, but H plasmas also occurred. Around 9.7×10^{24} N atoms, 4.0×10^{23} Ne atoms and 2.0×10^{25} Ar atoms were introduced during ILW-2, among other things for radiative plasma edge cooling and disruption mitigation [8]. Also notably, 0.48 barL of $^{18}O_2$ was injected into JET at the end of ILW-3 with the intention of providing a tracer for ex-situ analysis of component surfaces.

2.2. Analysis methods and data processing

All retrieved components were analysed with time-of-flight elastic recoil detection analysis (ToF-ERDA) using a 36 MeV $^{127}I^{8+}$ beam and the detection system described in Ref. [9]. Unless stated otherwise below, the geometry of the ToF-ERDA setup was such that both entry- and exit angles were 23±1° with respect to the sample surface. The energies of recoil ions were measured in a gas ionization chamber (GIC) filled with isobutane, typically at 45 mbar, and

flight time was measured over a distance of 400 mm. The system was used in what is referred to in Ref. [9] as full energy mode, i.e. measuring the full energy and flight time of recoil ions, except for the set of QMB covers retrieved from JET in 2014, for which partial energy signals were recorded using two anode segments in the GIC. The raw ToF-ERDA data from SB4-6 and QMB covers retrieved in 2014 was analysed with Potku [10] to produce elemental depth profiles. A compensation for detection efficiency was applied for species with mass less than 19u using values previously measured with the method described in Ref. [11]. Due to a bug occurring in version 1.0 of Potku when efficiencies for two isotopes of the same element are to be taken into account (here H and D), depth profiling was performed twice on each dataset including H but excluding D and vice versa. The depth profile thus generated for H was saved, as well as those for all other elements from the calculation including only D. These were then combined and renormalized with the condition that the average of the sum of all elemental fractions at depths between 10^{17} and 2×10^{18} at/cm^2 should be one. The depth scale, i.e. the thickness of each depth slab, was increased by the renormalization factor to preserve integrated values of atoms per unit area, which is the appropriate procedure under the approximation that H and D atoms present in the layer do not contribute towards stopping power. Raw ToF-ERDA data from SB8-9 and QMB covers retrieved in 2017 was processed with our own MATLAB code CONTES [12], updated to the here used version 15.3 at Uppsala University and KTH. Detection efficiency was taken into account in CONTES for all species, again with the method from Ref. [11]. The substrate signal from Inconel-600 in the SB was modelled as coming from a mixture of Ni and Cr for the analyses with CONTES and Potku. The signals from stainless steel components with mass close to Fe in the QMB covers were treated together as Fe. All depth profiles were integrated to produce the areal densities of deposited species reported here. Areal densities larger than 10^{15} at/cm^2 have been rounded to two significant figures, respecting the estimated measurement errors discussed in Section 4. In some cases values smaller than 10^{15} at/cm^2 are given for W. These have only one significant figure, as they are typically based on rather few collected counts (see for example Fig. 10 a).

The reason that Potku was chosen for some of the data processing despite the encountered isotope problem is that it allows for more convenient application of the same analysis procedure to several datasets than does CONTES. It also saves regions of interest and data from intermediate steps, which helps transparency and reproducibility. On samples from ILW-3, where ^{18}O was detected, we were not able to circumvent the isotope problem and had therefore to rely on CONTES. The results obtained when applying both programs to the same datasets have previously been compared and shown to be in agreement except for one variation. It is related to the different methods used for treating counts with energy higher than that of a recoil from the sample surface, which are present as a result of broadening of edges in the spectrum by finite detector resolution and/or an error in the time-of-flight calibration. Profiles calculated with Potku include such counts and therefore show tails extending to negative depth. CONTES, on the other hand, neglects the negative part of the profile but applies a normalization factor to each depth bin such that elemental fractions add up to unity. The normalization compensates the error introduced by neglecting counts unless the ToF calibration is severely off or the composition of the studied film changes drastically within the first 10^{17} at/cm^2 or so beneath the sample surface. For the present study, the difference between the analysis programs is not estimated to have given rise to any significant inconsistencies in the results.

Nuclear reaction analysis (NRA) was performed on selected components with a 2.8 MeV $^{3}He^{+}$ beam at normal incidence to obtain accurate values for the amount of D retained in the deposited layers per unit area, and to cross-check the ToF-ERDA results. The detector angle was approximately 172° for the NRA measurements on SB, and 167° for the measurements on QMB covers. Analysis of NRA data was carried out with SIMNRA [13]. An initial guess of the layer composition and thickness was made based on the ToF-ERDA result obtained at the point closest to the NRA measurement in question. The layer composition was then adapted in order to reproduce the signals from four reactions: $^{9}Be(^{3}He,p_1)^{11}B^{*}$, $^{9}Be(^{3}He,p_0)^{11}B$, $^{2}H(^{3}He,p)^{4}He$ and $W(^{3}He,^{3}He)W$, with proton energies 8.03 MeV, 9.84 MeV and 11.4 MeV for the former three and backscattered ^{3}He energy 2.62 MeV for the latter at 167°. Nuclear reaction cross sections from Ref. [14] and [15] as well as Rutherford backscattering from all detected elements, were used to calculate spectra. Measurement time (total ion fluence) and detector solid angle were taken into account by multiplying the calculated spectrum with a factor chosen such that the substrate signal was reproduced. The substrate was set as Inconel-600 (75.5 at.% Ni, 15.5 at.% Cr, 8 at.% Fe and 1 at.% Mn) for the SB, while Fe was used to represent stainless steel for the QMB covers similarly to what was done in the ToF-ERDA analysis. The condition for considering signals to have been reproduced is here that the total number of counts in the peaks corresponding to the four studied reactions should be the same in the measured and calculated spectra. As such, the NRA (with Rutherford backscattering, RBS) measurements give areal densities of D, Be and W. Representative examples of ToF-ERDA and NRA spectra from QMB covers from ILW-3 and SB6 from ILW-1 are given in Fig. 1 and 2. The latter also shows the calculated SIMNRA spectrum after D, Be and W fractions were adapted.

Surface morphology and the presence of dust particles on SB4-6 were studied by scanning electron microscopy (SEM) using a Hitachi SU8000 FE-SEM. 5 and 10 keV primary beams were used while secondary electrons and backscattered electrons (BSE) were detected. Energy-dispersive X-ray spectroscopy (EDS) was performed in the same setup, also with 5 and 10 keV primary electron energies and a Thermo Fisher Scientific UltraDry detector.

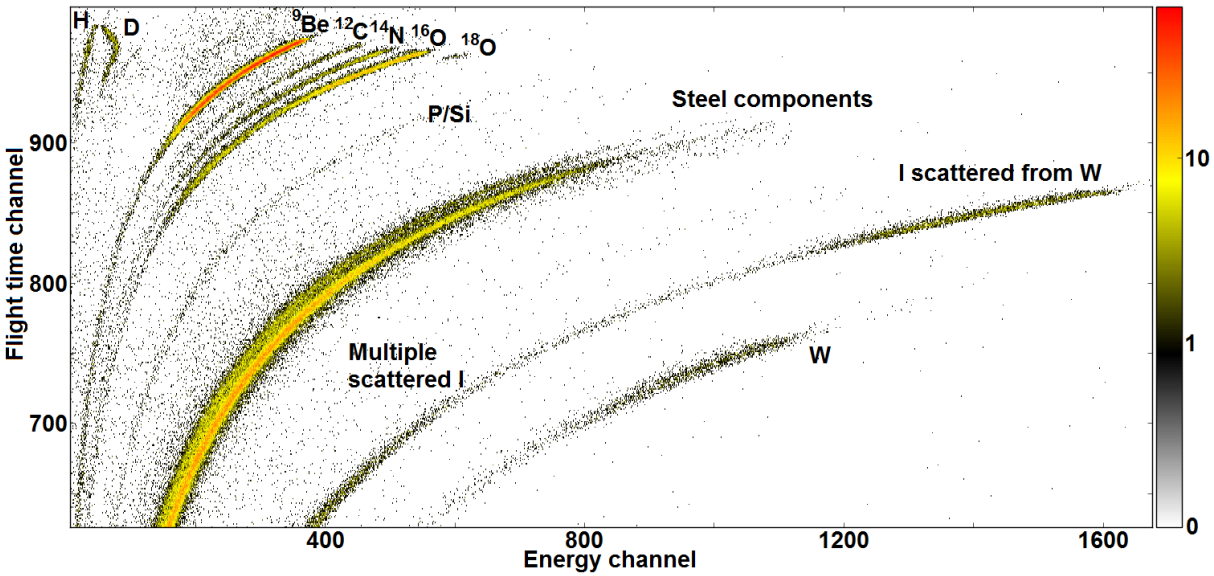

Figure 1: Added ToF-ERDA spectra from QMB covers 3 and 5 from ILW-3 indicating all signals detected when using the gas ionization chamber detector in full energy mode. The rather faint signal seen between ^{18}O and the steel components around the mass of Fe is a combination of counts from Si and P which are also present in the steel. Due to the small fraction of these elements (on the order of 1 at.%) and the density of background counts, we estimate that inclusion of the signal in the analysis does not improve the quality of any results. It has, therefore, been ignored. The reason for the unusual shape of the D signal is that only half the total anode length in the gas ionization chamber was used to measure energy. The highest energy D recoils were not fully stopped over the anode, and thus only a fraction of their energy was recorded. The depth profiling is not affected, since it uses the measured flight time rather than the energy.

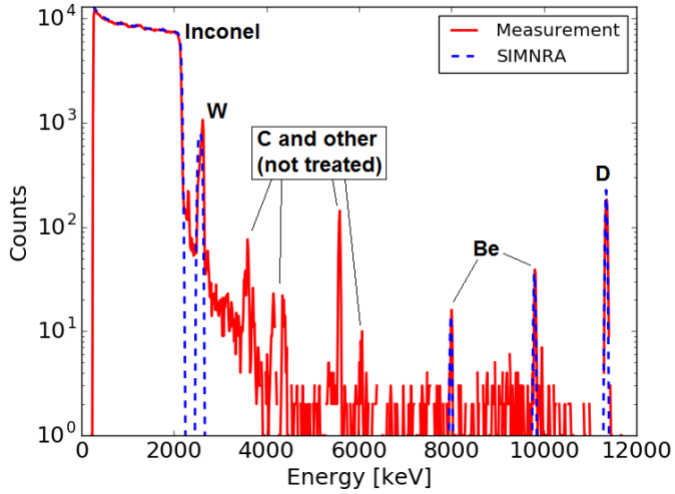

Figure 2: NRA spectrum and SIMNRA calculation from SB6 from ILW-1. Nuclear reactions with D and Be, as well as backscattering from all deposited species and the Inconel-600 substrate were included in the analysis.

3. Results

3.1. Spatial blocks 4-6 from ILW-1

ToF-ERDA measurements were performed on three sides of SB4-6: the side facing towards the plasma, the opposite one facing away from the plasma (referred to below as the backside) and one of the sides 90° from the plasma facing direction, opposite to the side fastened on the divertor carrier rib. The geometry of the ToF-ERDA setup was modified for the measurement on the side facing 90° from the plasma; entry angle was 30° and exit angle 15°. Deposited layers whose thickness decreased with the distance from the plasma facing side were observed. Several measurements were performed in order to quantify this decrease. In addition, a few NRA measurements were performed on each block. Fig. 3 shows the deposited layer thickness measured with ToF-ERDA as the depth at which the atomic fraction of the major component of the layer (Be, O or C) goes below that of Ni from the Inconel-600 substrate. The depth unit of atoms per unit area has been translated to actual sample depth using the average interatomic distance in BeO, i.e. 0.6899 Å/(10^{15} at/cm^2). This is a very crude approximation of the layer density, since (i) the layers contain many elements other than Be and O, and (ii) stratified deposits such as these (see Section 3.5) likely have a porous structure that is less dense on

average than a pure crystalline sample of BeO. The layer thicknesses given here should therefore be read as lower limits that give a sense of the involved orders of magnitude. The values could in reality be higher by several tens of percent. While the different compositions of the layers make comparisons between Fig. 3 a, b and c possibly misleading, the variation of the layer density across each block is small enough that we estimate the measured trend of decreasing layer thickness with increasing distance from the plasma facing side to be accurate. Comparisons between different samples should be made primarily based on numbers given in terms of areal densities. Photographs, oriented such that the plasma facing direction is towards the left in the image are overlain in Fig. 3. The black or discoloured ovals show the ToF-ERDA measurement spots while red crosses indicate NRA points.

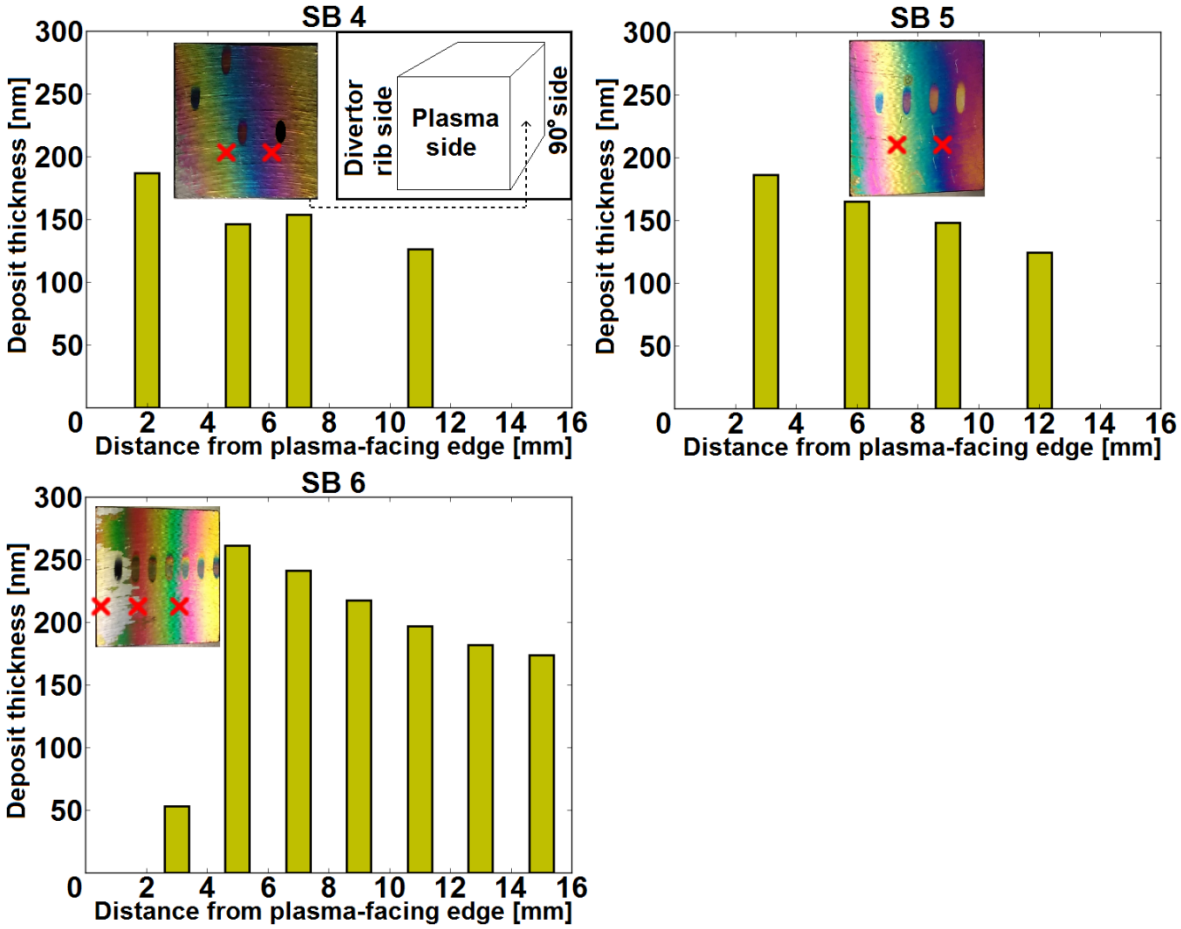

Figure 3: Side 90° from plasma facing direction on SB4-6 from ILW-1. Layer thickness, measured as the depth at which the fraction of the major component of the deposited layer (Be, C or O) goes below the Ni fraction from the Inconel-600 substrate by ToF-ERDA, is given by the bar plots. The recalculation from areal density to layer thickness was performed assuming the density of BeO, which results in a lower bound estimation. The black or miscoloured oval marks are the ToF-ERDA spots as seen after the measurement was performed and the images are oriented such that these marks appear in the same order from left to right as the thickness-indicating bars. The rightmost mark on SB4 was emphasized with a black overlay. Red crosses correspond to measurement points for NRA. An inlay in the first plot shows the position of the analysed side of the block with respect to the plasma facing direction and the side fastened to the divertor carrier rib.

Fig. 4 a shows depth profiles for detected species from SB5, which are representative for all measurements on the side 90° from the plasma facing direction on SB4-5. Be and O are the main constituents of the deposited layer here and the atomic fractions of the two are similar. C occurs primarily deeper in the deposits, closer to the layer-substrate interface, where its atomic fraction increases toward 30-40 at.%. On SB6, the C fraction in the layer is significantly higher and a peak appears close to the surface, as seen in Fig. 4 b. Areal densities of all detected species are given in Table 1. In order to provide comparative numbers for the areal densities measured with ToF-ERDA and NRA, each NRA result is presented on the same line in the table as that from the closest ToF-ERDA point. In the case where an NRA point lies between or close to two ToF-ERDA points, the values from those points have been averaged and the positions of both points are given. Due to ion-induced release of diatomic gases during the ToF-ERDA measurement, the areal densities of especially H and D are underestimated. This effect can be compensated for by comparing the signal from the species in question to that from the substrate, which is assumed to only vary with beam current. The function suggested by Adel et al. [16] is fitted to the evolution of the ratio of these signals' intensities over the course of the measurement. A compensation factor for the areal density is then produced as the ratio of the average value of the fit over the whole measurement to the initial value. An example of a fit of this kind for D on SB6 is shown in Fig. 5. The point from which the curve was produced is the one where the largest effect has been recorded, and the value of the compensation factor is 3.52. Factors of 1.41 and above were found for all points included in Table 1, where the compensated values of the areal density of D are reported. The uncompensated values are given in parentheses. This dataset is the only one in the present study for which ion-induced release compensation has been applied, and as such the reported values for H and D densities in later sections should be read as lower limits rather than exact values. The numbers are, however relevant for qualitative comparison of the D retention at different points. The ratio of the D signal to that from the substrate was also examined for the NRA measurements, but no detectible reduction over time was seen. It has therefore been concluded that significant ion-induced release of D has not occurred during any of the NRA measurements presented in this work. A discussion on ion-induced release of H isotopes due to ^{3}He bombardment at higher fluences is given in Ref. [17] and [18]. As seen in Fig. 1, there are two available signals for calculating the W density from ToF-ERDA; by using either forward scattered primary ^{127}I ions or W recoils. These yield similar numbers and both are given in Table 1, the former in parentheses.

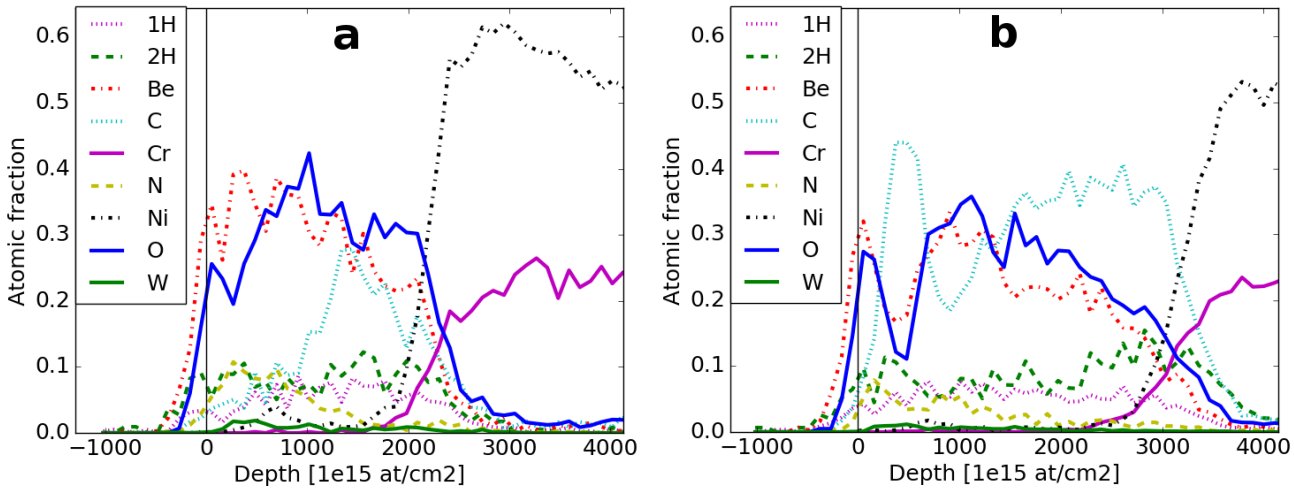

Figure 4: ToF-ERDA depth profiles from (a) the 9 mm point 90° from plasma facing direction on SB5, and (b) 9 mm point 90° from plasma facing direction on SB6, both from ILW-1.

	Position [mm]		Areal density, ERDA [10^{15} at/cm^2]							NRA [10^{15} at/cm^2]		
Sample	**ERDA**	**NRA**	**H**	**D**	**^{9}Be**	**^{12}C**	**^{14}N**	**^{16}O**	**W**	**D**	**Be**	**W***
SB4	11	10	120	320 (210)	770	250	120	680	18 (17)	370	740	20
	5, 7	5	150	360 (240)	830	370	110	780	23 (24)	560	790	23
SB5	9	10	160	440 (250)	780	390	120	810	21 (22)	420	770	19
	6	5	210	490 (260)	850	510	120	880	22 (26)	550	800	24
SB6	9,11	10	190	800 (350)	730	1100	92	830	15 (15)	880	770	16
	5	5	240	1600 (460)	830	1500	110	930	17 (17)	1200	920	18
	3	1	36	240 (140)	210	460	14	250	2.7 (2.9)	460	180	3.4
Estimated relative error [%]			**	50	30	30	40**	40**	30	10	10	10

Table 1: Areal densities of all species measured on the side 90° from the plasma facing direction on SB4-6 from ILW-1. Positions are given as approximate distances in mm from the edge of the plasma-facing side. In the cases where two points are given for ToF-ERDA, the results from those points have been averaged. Numbers in parenthesis indicate values before ion-induced release compensation for D and values calculated from the scattered ^{127}I signal for W. Integration depth for ToF-ERDA: 5×10^{18} at/cm^2 including entire deposited layer. See Section 4 for details on the estimated relative errors given for each column in the bottom row. *The W signal from the NRA measurement comes from backscattered ^{3}He (RBS signal). **Reported numbers for H, N and O are without compensation for ion-induced release. The actual values may therefore be higher, in particular for H, as discussed in the present section as well as Section 4.

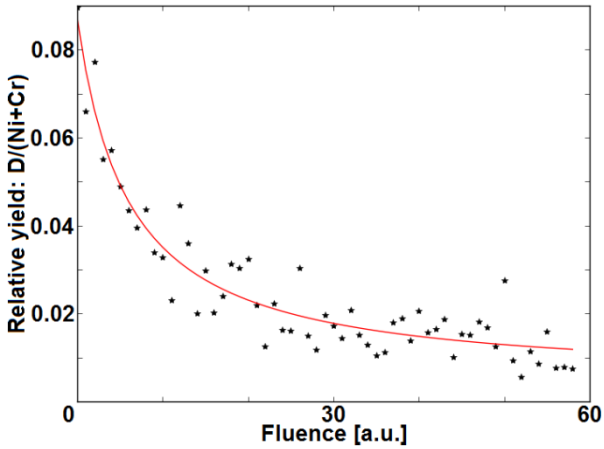

Figure 5: Ion-induced release of D during the ToF-ERDA measurement from the 5 mm point on SB6 from ILW-1.

Photographs of the deposits on the plasma facing and backsides of SB4-6 are shown in Fig. 6. Two ToF-ERDA measurement points were selected along a vertical line in the middle of each of these sides. The first measurement was performed at a lower point, about 5 mm from the bottom edge of the block as seen in the image, and the second measurement at an upper point, about 10 mm from the edge. Due to the orientation of the blocks in the ToF-ERDA setup, larger numbers for the position here, i.e. the upwards direction in Fig. 6, corresponds to the

downward direction in the JET divertor. Integrated areal densities are reported in Table 2. The integration depth was 4×10^{18} at/cm^2 on the side facing away from the plasma, which was enough to include the entire deposited layer in all measured points. On the plasma-facing sides of SB4-5, the layer is thick enough that the Inconel-600 substrate can just barely be seen in the ToF-ERDA spectrum (suggesting a layer thickness on the order of 8×10^{18} at/cm^2 or roughly 600 nm). On the plasma facing side of SB6 the substrate could not be detected at all and the layer is thus thicker than 10^{19} at/cm^2, i.e. at least around 1 µm. It is difficult to correctly identify counts for some elements in the deepest part of these thick layers. For example, ^{14}N may be misattributed to ^{16}O or ^{12}C below approximately 7×10^{18} at/cm^2. In addition, the signal from H is below the lower level discrimination set to eliminate noise in the energy detector for counts originating from depths larger than around 8×10^{18} at/cm^2. For these reasons, the integration depth for the thicker layers on the plasma-facing side was set to 6×10^{18} at/cm^2, and the reported numbers are thus indicative for the composition of the layers down to that depth.

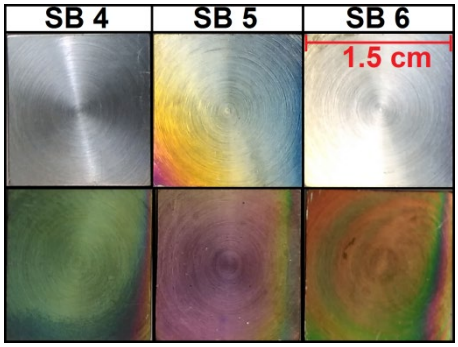

Figure 6: Plasma-facing (lower images) and back (upper images) sides of SB4-6 from ILW-1. The images are oriented such that the third measured side, 90° from the plasma facing direction is to the left. The vertical orientation reflects the mounting of the samples in the ToF-ERDA setup, and upwards in the image therefore corresponds to the downwards direction in the JET divertor.

		Areal density, ERDA [10^{15} at/cm^2]						
Sample	**Position [mm]**	**H**	**D**	**^{9}Be**	**^{12}C**	**^{14}N**	**^{16}O**	**W**
SB 4, plasma side	10*	600	750	2000	870	300	1400	77
	5*	580	840	2400	940	350	1400	79
SB 4, backside	10	51	59	430	87	62	490	2.0
	5	57	46	480	110	66	490	1.6
SB 5, plasma side	10*	690	710	2000	970	320	1500	62
	5*	650	830	2100	970	340	1500	76
SB 5, backside	10	68	84	460	170	74	470	5.0
	5	97	140	490	280	91	510	3.7
SB 6, plasma side	10*	780	890	2000	1300	310	1600	59
	5*	730	970	1900	1100	300	1500	60
SB 6, backside	10	58	91	360	170	49	450	1.6
	5	59	74	360	160	45	400	2.4
Estimated relative error [%]		**	**	30	30	40**	40**	30

Table 2: Areal densities of species detected on the plasma facing and back sides of SB4-6 from

ILW-1. Integration depth 4×10^{18} at/cm^2 including entire deposited layer; $^{*}6\times10^{18}$ at/cm^2 not including entire layer. Increasing position values correspond to the downward direction in the divertor. **Reported numbers are without compensation for ion-induced release. The actual values for H and D may therefore be several times higher than indicated.

Fig. 7 shows one depth profile from the plasma facing side of SB6 and one from the backside of SB5. In Fig. 7 b, we note that the thin layers deposited on the backsides of the blocks are primarily made up of Be and O, with around 10 at.% or less of H, D, C and N. The amount of W is negligible. These features are representative for all measured points on the backsides of SB4-6. The C fraction increases up to between 20 and 30 at.% close to the interface between the layer and the Inconel-600 substrate on SB5-6, similarly to what was observed on the 90° side of SB4-5, while on SB4 the C concentration on the backside remains low throughout the layer. On the plasma-facing side, a peak in the C fraction is seen close to the surface for all measured points. The C content in these layers is generally high; above 10 at.% up to 30 at.%. An increase of the C fraction to over 40 at.% coincides with an increase of the D fraction at depths beneath 6×10^{18} at/cm^2 on SB6, as seen in Fig. 7 a. The increase is real, and not due to a misattribution of counts, which can be verified by studying the raw data shown in Fig. 8. The increased intensity of the C signal here occurs in a region where there is no risk of misattributing a significant fraction of Be or O counts as C. It is difficult to assess in this case whether H behaves similarly as D, since the increase of the signal intensity occurs at a depth for which the H signal is lost due to lower level discrimination as described above. High fractions of both H and D are found on the plasma facing sides of the blocks, typically between 10 at. % and 20 at.% without compensation for ion-induced release.

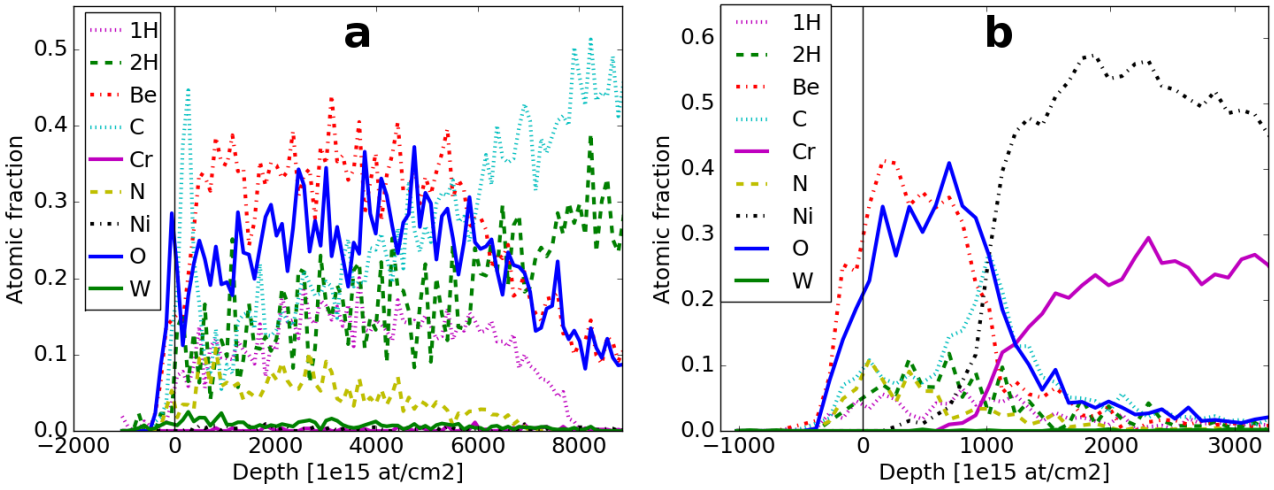

Figure 7: ToF-ERDA depth profiles from (a) the 10 mm point on the plasma-facing side of SB6, and (b) the 5 mm point on the backside of SB5, both from ILW-1. The complete loss of the H signal around 8×10^{18} at/cm^2 is an artifact due to the lower level discrimination for noise elimination set for the gas ionization chamber used to record energy.

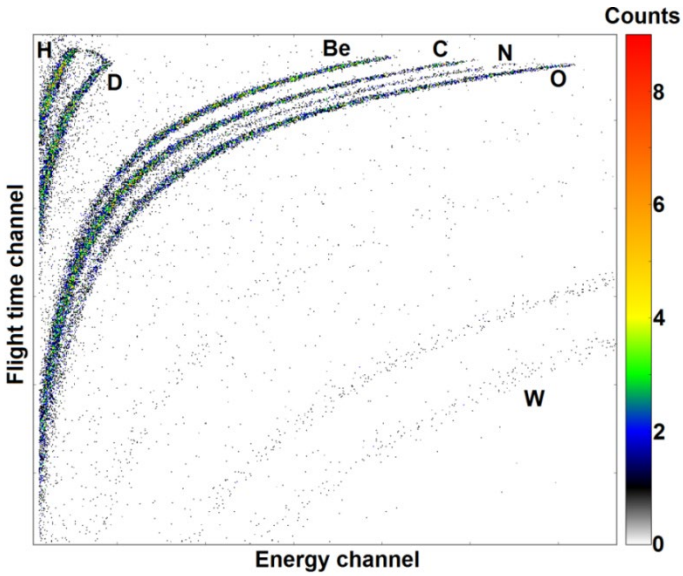

Figure 8: ToF-ERDA spectrum from the 10 mm point on the plasma-facing side of SB6 from ILW-1. The displayed region is selected to show the full H, D, Be, C, N and O signals. Only a faint, almost undetectable signal from the substrate is present, as the deposit is thicker than the ToF-ERDA information depth of approximately 1 μm.

3.2. QMB covers 1-3 and 5 from ILW-1-2

NRA and ToF-ERDA measurements were performed in 4-6 points on each QMB cover from ILW-1-2. Fig. 9 shows the positions of these points. The parts of the covers pointing downwards in the figure were also pointing downwards in the divertor and were thus exposed at a position similar to the SB, while the upper parts were partially shadowed behind Tile 3 or 7. The lower regions around the hole through which the QMB crystals are normally exposed were covered by a shutter which was permanently closed due to a malfunction after approximately 100 pulses in ILW-2. The edge of the shutter covered region can be seen as a diagonal line in each photograph. Table 3 gives the areal densities of detected species with distances given from the top of the image, so that larger values correspond to the downward direction in the divertor, as for the spatial blocks in Section 3.1.

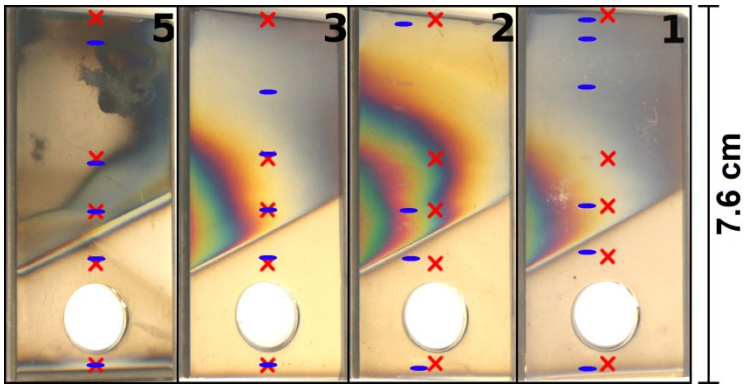

Figure 9: QMB covers from ILW-1-2. Dark blue ovals indicate the positions of ToF-ERDA measurement points while red crosses indicate NRA points.

As noted in Section 2.2, ToF-ERDA was performed differently on the QMB covers from ILW-1-2 than on the other components included in the present study. Instead of only measuring the two signals for flight time and energy, three signals were recorded: flight time and two partial energy signals. The partial energy signals were recorded with two anode segments in the GIC, covering the first 47 mm and the subsequent 169 mm of the paths of ions being stopped in 15 mbar isobutane. For high energy and/or light ions the signal from the first anode segment is close to proportional to the stopping power of the ion in question in the detection gas, whereas for lower energy or heavier ions that are fully stopped over 47 mm, the full energy signal is produced. In Fig. 10 a, a scatter plot of data from QMB1 is shown, with the first anode signal on the y-axis and the flight time signal on the x-axis. The same data is shown in Fig. 10 b but with flight time on the y-axis and the full energy signal, obtained by adding the signals from the anode segments, on the x-axis. A further discussion on the difference between the two methods of signal separation and the consequences for data interpretation can be found in Section 4. The stopping power based separation from Fig. 10 a was used for the reported areal densities. Note that the H and D signals have been lost due to the low detection gas pressure in this case and we therefore have to rely on the NRA data for the quantification of D.

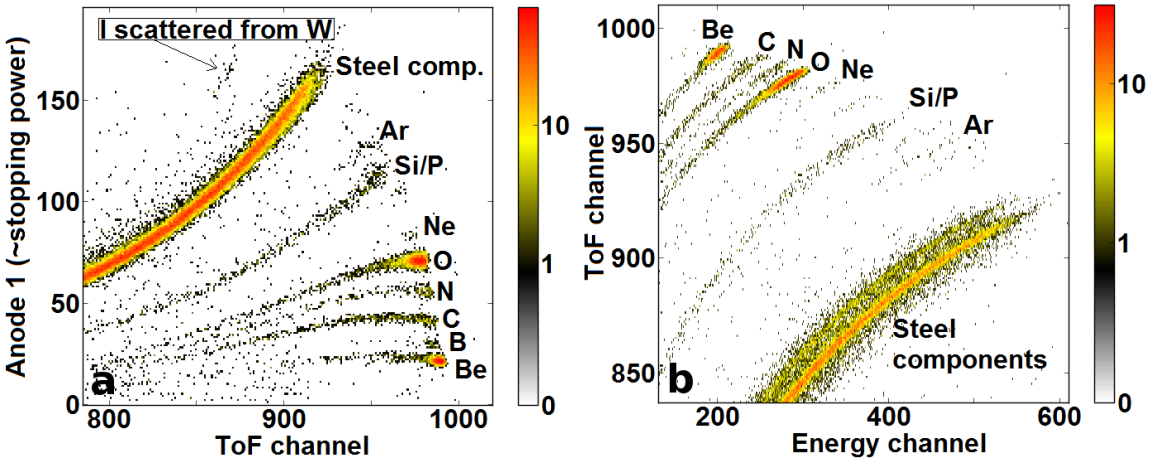

Figure 10: Comparison of ToF-ERDA signal separation with time-of-flight plotted against the anode signal from the first segment in the GIC (left) and the full energy signal (right). Data is from the 74 mm point on QMB1 from ILW-1-2 and the full energy signal was constructed as the sum of the signals from the two used anode segments. In this particular case the signal labelled Si/P, which is assumed to come from the content of those elements in the stainless steel substrate, shows an increased density of counts in the region corresponding to the first 100 nm below the surface. The concentration of Si, or some element close to it in mass, would therefore seem to have increased from little over 1 at.% in the bulk to between 2 and 4 at.% in the film. This is not observed on any other sample, but could potentially be due to the presence of a small quantity Al originating from the remote handling equipment in JET.

	Position [mm]		Areal density, ERDA [10^{15} at/cm^2]					NRA [10^{15} at/cm^2]		
Sample	**ERDA**	**NRA**	**Be**	**C**	**N**	**O**	**W***	**D**	**Be**	**W***
QMB1	2	1	440	47	95	440	5.7	63	300	2.9
	6	-	440	57	130	430	4.1			
	16	30	460	82	98	500	8.1	150	460	17
	41	41	840	56	150	710	15	210	650	14
	51	52	47	16	29	95	0.5	1.8	20	-
	74	73	230	57	35	340	1.0	16	190	1.2
QMB2	2	1	920	160	260	710	12	88	540	4.6
	-	30						420	1100	41
	41	41	1500	160	290	1200	33	410	1200	26
	51	52	140	33	34	130	0.3	9.3	80	0.7
	74	73	150	16	41	220	-	18	180	0.9
QMB3	16	1	570	59	130	480	11	69	330	2.5
	29	30	780	120	160	670	30	140	560	22
	41	41	1100	64	200	830	24	260	770	17
	51	52	32	10	23	55	0.5	-	-	-
	74	73	170	28	40	250	0.6	10	46	0.5
QMB5	6	1	240	3300	68	200	2.3	44	210	3.7
	31	30	300	33	40	140	6.2	11	180	4.8
	41	41	880	29	84	460	13	130	860	11
	51	52	190	13	27	160	0.9	9.3	120	1.0
	73	73	960	41	150	620	1.7	230	1000	2.1
Estimated relative error [%]			30	30	40**	40**	30	10	10	10

Table 3: Areal densities of species detected on QMB covers from ILW-1-2. Ar, Ne and B densities are smaller than 10^{16} at/cm^2 in all points; which is not considered enough for reliable quantification in this case. These elements are therefore not included. Integration depth for ToF-ERDA: 5×10^{18} at/cm^2 including entire deposited layer, except for the point at 6 mm on QMB5 where a C structure thicker than 1 μm is present, as seen in Fig. 9. A part of the beam spot was hitting that structure, which is why C is measured to be the primary layer constituent at the point in question. *W signal from scattered ^{127}I for ToF-ERDA, backscattered ^{3}He (RBS signal) for NRA. **Reported numbers are without compensation for ion-induced release.

Two depth profiles that are representative of the layer composition for all measured points on the QMB covers from ILW-1-2, except the 6 mm point on QMB5, are given in Fig. 11. It is worth noting here that the cover from QMB1 has a similarly composed deposit on it as the covers from QMB 2, 3 and 5, even though the former was present in JET during ILW 1-2 while the latter three were present only during ILW-2. This is an example of the fact that the composition of a deposited layer on a plasma-facing component depends primarily on the most recent operation history, while longer term information may be found in deeper parts, especially of thick deposits. Another observation is that the QMB covers have significantly less C on them than the SB. The difference can be explained by the fact that the SB are mounted

directly on the C ribs of the divertor carrier, while the QMB covers are mounted between the ribs, as illustrated in Ref. [7].

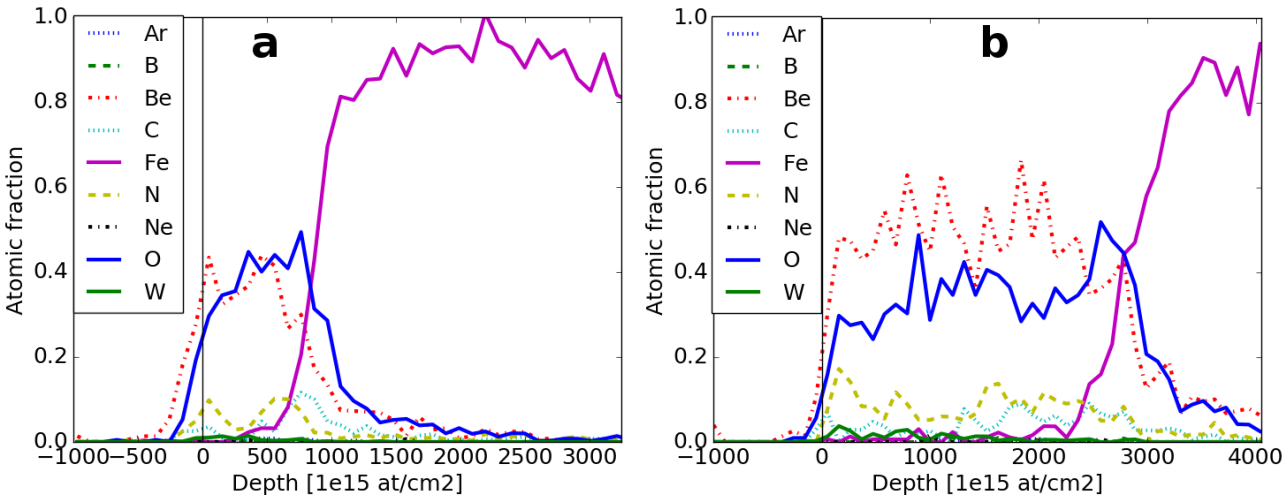

Figure 11: ToF-ERDA depth profiles from (a) thinner layer at point 16 mm on QMB1 from ILW-1-2, and (b) thicker layer at point 41 mm on QMB2 from ILW-2.

3.3. Spatial blocks 8-9 from ILW-3

The plasma-facing and 90° sides of SB8-9 were analysed in two points each with ToF-ERDA. The points were selected similarly to those from the plasma facing and back sides of SB4-6; an upper point and a lower point 5 and 10 mm from one edge of the block. In this case, the orientation of the blocks in the ToF-ERDA setup was such that the two points on the 90° side were equally far (~7.5 mm) from the plasma facing side, but at different heights. Areal densities are given in Table 4. As in previous sections, the position value given in the table increases for points further down in the divertor.

		Areal density, ERDA [10^{15} at/cm^2]							
Sample	**Position [mm]**	**H**	**D**	**^{9}Be**	**^{12}C**	**^{14}N**	**^{16}O**	**^{18}O**	**W**
SB 8, plasma side	10**	230	410	1900	940	310	1700	14	150
	5**	170	480	2300	460	360	1900	16	260
SB 8, 90° side	10	95	130	1100	590	160	1400	9.6	81
	5	100	170	1100	600	170	1400	11	81
SB 9, plasma side	10**	190	420	2100	760	320	1800	10	200
	5**	190	430	2200	680	340	1900	15	220
SB 9, 90° side	10*	110	120	1300	890	180	1700	6.2	87
	5*	95	140	1300	910	180	1700	6.8	86
Estimated relative error [%]		***	***	30	30	60***	60***	***	30

Table 4: Areal densities of species detected on SB8-9 from ILW-3. Integration depth 5×10^{18} at/cm^2 including entire deposited layer; *6×10^{18} at/cm^2 including entire layer; **6×10^{18} at/cm^2 not including entire layer. ***Reported numbers are without compensation for ion-induced release. The actual values for H and D may therefore be several times higher than indicated. Factors up to 2.2 were noted for ^{18}O (see Section 4).

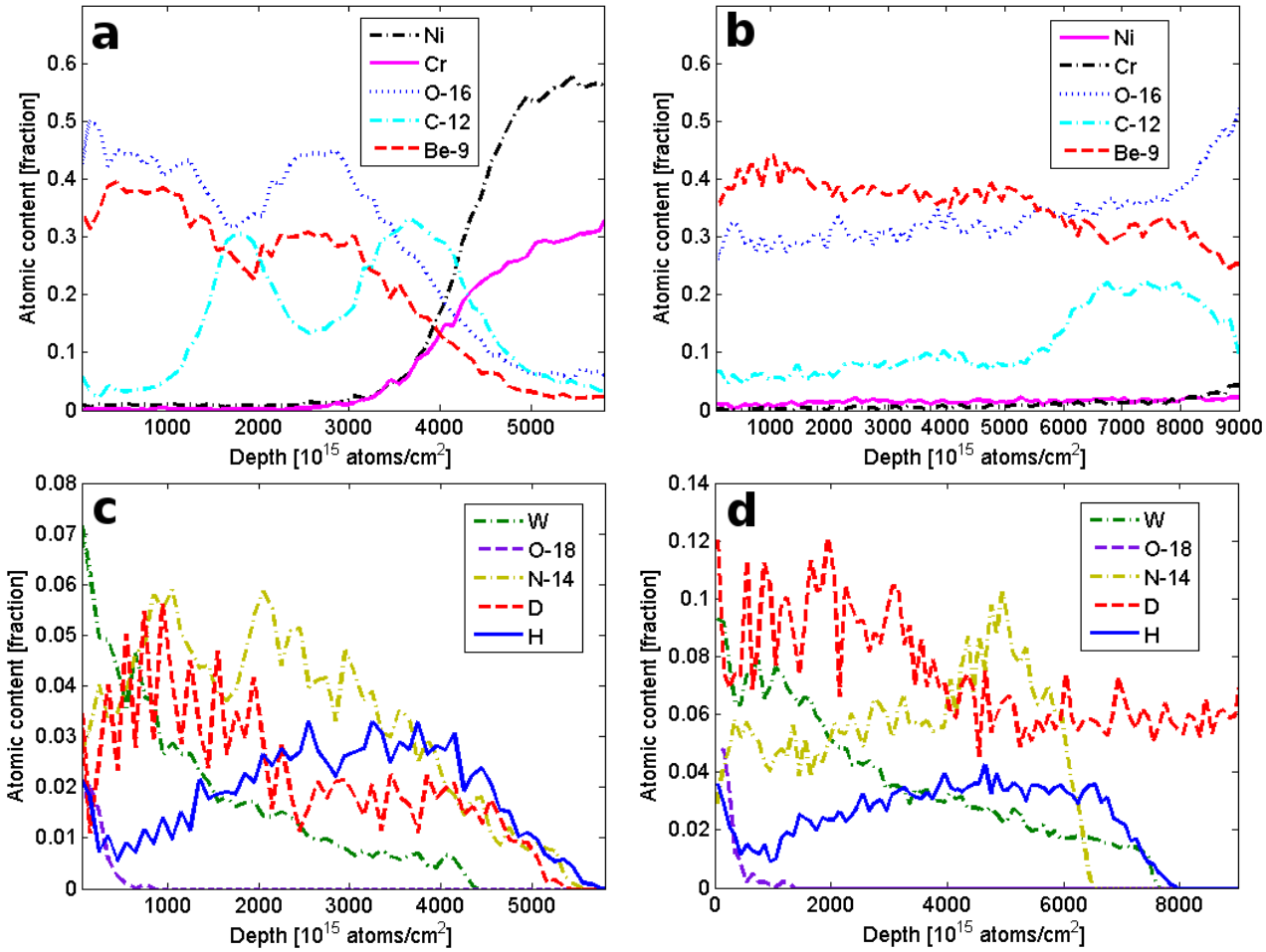

Figure 12: ToF-ERDA depth profiles for major (a, b) and minor (c, d) constituents of the layer deposited at the 10 mm point, 90° from the plasma facing side of SB9 (a, c) and the 5 mm point on the plasma facing side of SB8 (b, d), all from ILW-3. The abrupt loss of the N, W and H signals between 6×10^{18} at/cm^2 and 8×10^{18} at/cm^2 are artifacts due to misattribution of counts and lower level discrimination for noise suppression in the flight time and energy detectors.

Fig. 12 gives representative depth profiles for all elements found on SB8-9. The W fraction on these blocks increases from around 1-2 at.% in the deeper parts of the layers to between 5 and 8 at.% close to the surface. H and D are more evenly distributed throughout the layer, but with a trend towards decreasing H fraction and increasing D fraction close to the surface. The C fraction on the side 90° from the plasma-facing direction shows one peak close to the layer-substrate interface on SB8, and two peaks on SB9 as seen Fig. 12 a. On the plasma facing side, the layer is thick enough so that the substrate signal is only barely visible in most points, i.e. around 8×10^{18} at/cm^2, except for the 10 mm point on SB8 where a thick interface with slowly increasing Ni and Cr signals is seen from a depth of approximately 5×10^{18} at/cm^2.

3.4. QMB covers 1-3 and 5 from ILW-3

Four points, as shown in Fig. 13, were selected for ToF-ERDA measurements on the QMB covers from ILW-3. Table 5 gives the areal densities of all detected species in these points.

Positions are given as in previous sections with higher values in the downward direction. Note that the reference position "0 mm" is about 3 mm from the upper edge of the plate here, in contrast to the QMB covers from ILW-1-2 in Table 3 where the reference position is at the edge. The shutter was functioning properly for QMBs 1, 2 and 3 during ILW-3, and was open during 19 500 s, 25 700 s and 28 200 s respectively for those units. Ref. [5] gives further information on how the QMB cover is shielded from particle impacts by the shutter in the open and closed states. For QMB5, the shutter was opened permanently early in ILW-3 (halfway into the JET C35 campaign), and the open shutter time was therefore only a little less than the total divertor plasma time of ~67 000 s. Fig. 14 shows representative depth profiles from QMB3. The large Be fraction seen in the figure is measured in most points on the QMB covers from ILW-3. While all other studied components have shown similar amounts of Be and O, we here see up to several times more Be than O. An especially Be-rich deposit is present at the 41 mm point on QMB5, with around 70 at.% of Be throughout the entire layer thickness of approximately 5×10^{18} at/cm^2. A high atomic fraction of D is measured, typically between 10 and 20 at.% without ion-induced release compensation. This is higher than what is seen on SB from ILW-3, but similar to the levels in the C rich layers on SB from ILW-1.

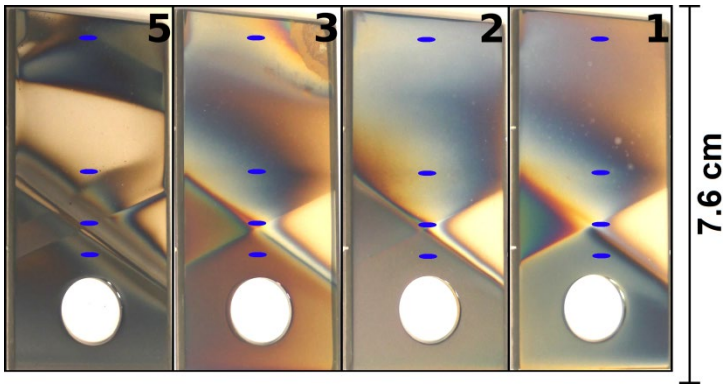

Figure 13: Stainless steel covers for quartz microbalance deposition monitors from ILW-3. Dark blue ovals indicate the positions of ToF-ERDA measurement points.

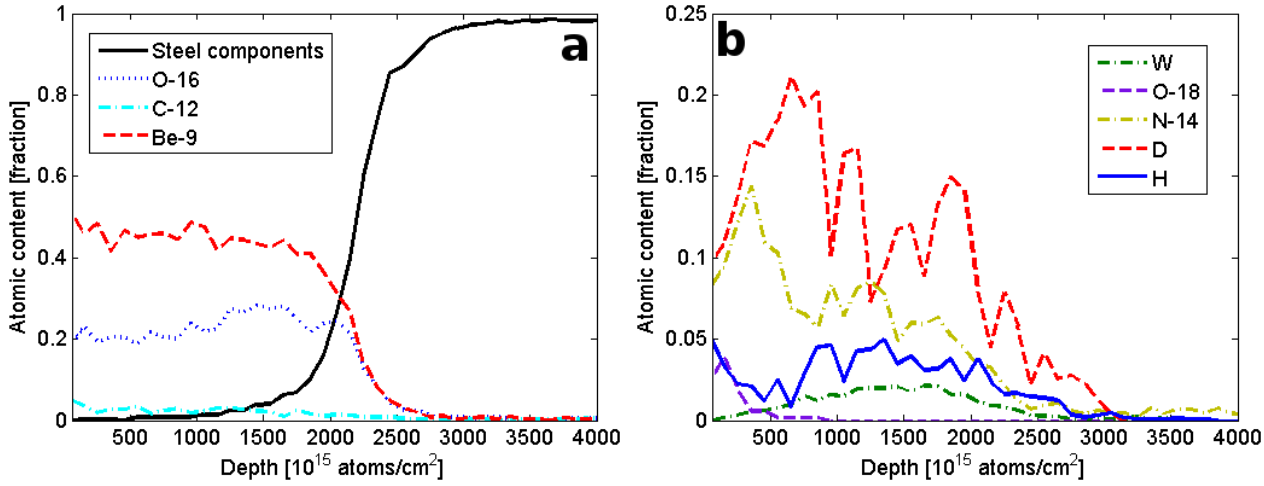

Figure 14: Depth profiles of (a) major and (b) minor constituents of the layer deposited at the 41 mm point on the cover of QMB3 from ILW-3.

		Areal density, ERDA [10^{15} at/cm^2]							
Sample	**Position [mm]**	**H**	**D**	**^{9}Be**	**^{12}C**	**^{14}N**	**^{16}O**	**^{18}O**	**W**
QMB1	1	25	110	420	16	83	310	-	5.7
	30	14	120	470	50	56	390	-	62
	41	50	220	890	54	140	560	12	31
	48*	17	130	510	53	72	350	21	48
QMB2	1	38	85	570	53	140	360	-	11
	30	40	180	600	74	79	460	-	78
	41	72	300	880	63	200	500	15	25
	48	90	340	1200	170	160	580	19	170
QMB3	1	41	120	370	140	76	300	-	4.7
	30	18	100	410	43	59	350	-	47
	41	80	320	990	58	180	540	10	32
	48	31	250	860	94	110	510	18	110
QMB5	1	43	80	640	23	100	180	-	1.7
	30	30	14	240	33	47	120	-	4.8
	41**	96	430	3600	63	240	740	-	9.2
	48	17	160	790	63	36	380	19	34
Estimated relative error [%]		***	***	30	30	40***	40***	40***	30

Table 5: Areal densities of species detected on QMB covers from ILW-3. Integration depth 4×10^{18} at/cm^2 including entire deposited layer; *3×10^{18} at/cm^2 including entire layer; **6×10^{18} at/cm^2 including entire layer. ***Reported numbers are without compensation for ion-induced release. The actual values for H and D may therefore be several times higher than indicated.

3.5 Electron microscopy on SB4-6 from ILW-1

Selected SEM images using the secondary electron signal on SB4 and SB6 are shown in Fig. 15. Peeling stratified deposits with at least five sublayers are visible in several places and exemplified in Fig. 15 a. Holes caused by detaching blisters and stress in the layer have also been found. Deposits in C-rich regions are similar to those that have previously been found in JET with carbon wall [19]. In the BSE images, a dense collection of Cu particles was seen on the side 90° from the plasma facing direction on SB6 with sizes from tens or hundreds of nm up to little over 1 μm and areal density on the order of 10^4 particles/mm^2. The EDS data showed W particles and a few Mo particles in the size range from a few hundred nm to around 1 μm. It further revealed pronounced signals from Be, C, N, O and W in line with the ToF-ERDA results.

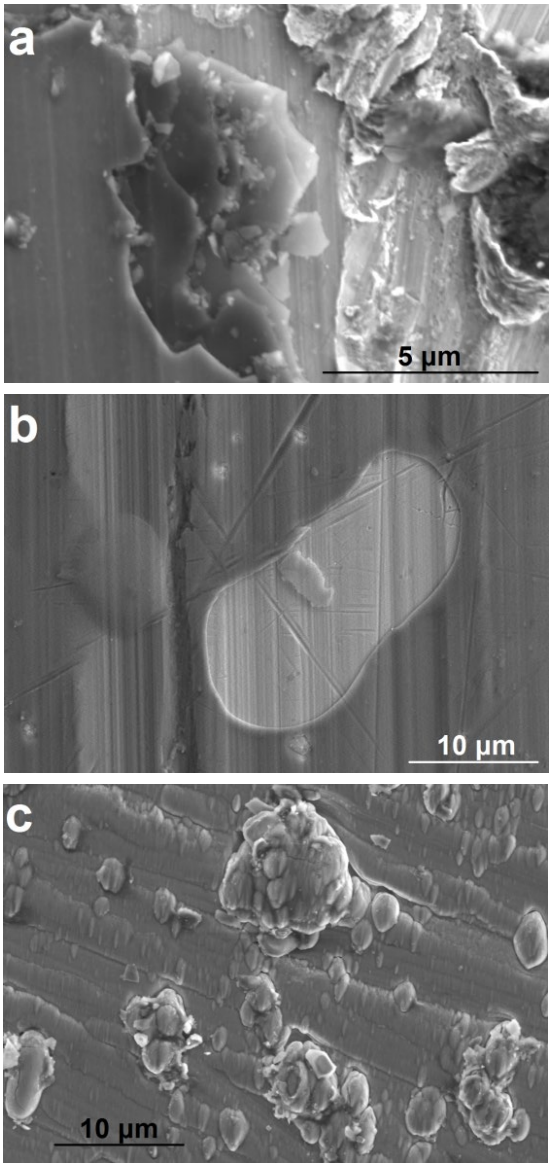

Figure 15: SEM-SE images of SB from ILW-1 showing (a) a stratified structure on SB4, (b) a blister that has formed on SB4 and later detached due to thermal and mechanical stress in the deposited layer, and (c) a C-rich deposit on SB6.

4. Discussion

As stated in Section 3.1, out of all ToF-ERDA results presented here, only those from the 90° side of SB4-6 were compensated for ion-induced gas release. The results for D in Table 1 show that when such compensation is applied along with detection efficiency compensation, quantitative agreement between NRA and ToF-ERDA is achieved. Ideally, all ToF-ERDA results for species that can leave the sample as diatomic gases (here H, D ^{14}N, ^{16}O and ^{18}O) should be compensated. This task is, however, rather cumbersome to carry out at present since available data conversion codes like Potku and Allegria [20] do not have the functionality built into their depth profiling routines. The compensation factor for ion-induced release is typically larger for light isotopes, like H and D, than for N and O. Even for the latter, however, factors

larger than two can be obtained as seen for example in Ref. [21]. In the present case, compensation factors were generated for ^{16}O on SB4-9, yielding values close to 1 on SB4, up to 1.3 on SB5-6 and up to 1.6 on SB9. The reported numbers for ^{14}N and ^{16}O in Tables 1-5 are without compensation and should therefore be read as lower bounds. When it comes to ^{18}O, no significant release was observed during the measurements on QMB covers from ILW-3. On SB from ILW-3, however, factors up to 2.2 were noted, and the corresponding values in Table 4 are thus underestimations as also stated in the table caption. The notable release of ^{18}O in this case could have to do with the fact that it is present primarily in the top few tens of nm and therefore is more easily released than ^{16}O which is found throughout the layer.

Significant uncertainties are present in the ToF-ERDA results even in the cases where ion-induced release has been taken into account. First there are uncertainties in stopping powers, which are imported from SRIM-2013 for the here used versions of CONTES and Potku. The provided values are similar to those from SRIM-2010 which have been reported to deviate on average between 3.5% and 5.6% from experimental data [22]. The deviation is typically small for light ions and increases for heavier ones. ^{127}I can therefore be estimated to lie at the higher end of the interval. To calculate stopping powers in compounds, *Bragg's rule* is used. It amounts simply to weighting the stopping powers from individual elements by their fractions in the material under study. The error resulting from the application of Bragg's rule, combined with the uncertainty in the stopping powers themselves, gives a total relative error up to 20%. This affects both the reported numbers for integrated areal densities and the depth scale for the profile plots. In the present case, since the chemistry of the deposits is unknown, the bonding corrections described in Ref. [22] can not be applied. Furthermore, data needed to perform such bonding corrections for Be are lacking. One should note, however, that since the studied deposits are of similar composition, the relative errors in the stopping powers should also be similar. A systematic deviation may thus be expected, indicating that variations in areal densities may be accurately measured even though the absolute values carry an error.

A second important error source is sample surface roughness. Especially if the angle between the surface and the incoming or outgoing trajectory is small, particles may pass through protruding structures. As the depth from which a recoil originates is calculated from the energy loss due to stopping, the added path traversed through such structures gives a false impression of depth. For this reason, layers may appear to be thicker than they actually are, resulting in an overestimation of the areal densities of their constituent elements. The surface roughness changes arbitrarily between different measurement points and the error is therefore of random magnitude.

The fact that both CONTES and Potku assumes single scattering may contribute further to the total error, as multiple scattering occurs especially for heavy elements at low energies. Multiple scattering can affect the interpretation of data pertaining to deeper parts of the studied layers, but is not expected to constitute a dominant error source in the present case. Statistical uncertainty from the Poisson distributed number of recorded counts in a channel influences the validity of the elemental fractions in individual bins of the depth profiles, but is not significant for the integrated areal densities. The fast oscillations in the profiles seen especially in Fig. 7 and 12 are a result of statistical uncertainty, possibly combined with artifacts from the binning itself. They should therefore not be interpreted as describing actual concentration variations in the samples. A final significant error source comes from the efficiency of the ToF detectors

which is almost constant for elements heavier than Li, but has been observed to fluctuate for H isotopes depending on the vacuum quality in the system. Absolute numbers for H and D concentrations are affected by this error while trends over a single measurement session are not. It is the case for each table given in this paper that all data points produced with the same method were recorded during the same session. As such, trends related to the variation of H and D concentrations are more reliable than the absolute numbers.

In conclusion, we expect an error up to approximately 30% for the depth scales and integrated areal densities measured by ToF-ERDA in this work in addition to the error related to ion-induced release. For H isotopes that error is even larger, estimated at 50% or more. D is more accurately measured with NRA in which case the dominating error comes from the uncertainty in stopping power through the applied criterion of reproducing the substrate signal. The uncertainty here is smaller than in the case of ERDA thanks to the lighter projectile. The approximation of an Fe substrate for the QMB covers also affects the stopping power. Finally, there may be a contribution from the nuclear reaction cross sections, as the values provided for Be were measured at 150°, which is smaller than the present detector angle by between 17° and 22°. It is not unreasonable to estimate that the resulting error in areal densities of D and Be measured with NRA on the QMB covers from ILW-1-2 and SB4-6 is on the order of 10%.

Since the samples included in this study have been stored after removal from JET, some for moths or even years, a relevant question is whether significant release of any element has occurred during storage. The most likely elements to undergo such release are noble gases, here Ne and Ar, that occur in deposited layers as trapped atoms. We can not assess or quantify the loss of noble gas atoms, and we thus conclude only that they may have occurred in concentrations higher than those indicated here when samples were initially retrieved from JET. For H isotopes the problem is smaller as they form chemical bonds in the deposits. Studies have previously been carried out to attempt to quantify the release of D over time from plasma-exposed samples. Ref. [23], for example, concludes that storage in air for three years leads to loss of 25-30% of retained D in co-deposits on a graphite plate while Ref. [24] reports a reduction of more than 50% of the H+D content in samples from the tokamak ASDEX after 272 days. The total effect of H/D isotope exchange in the present case is difficult to assess. That uncertainty adds to the total estimated error in the quantification of H and D discussed in the previous paragraph. Samples have been stored individually in sealed plastic containers without contact between the analysed surfaces and other materials or the container walls. Storage times between retrieval from JET and analysis were approximately 2 years for the QMB covers from ILW-1-2, almost 5 years for SB4-6 and 1 year for SB8-9 and QMB covers from ILW-3. It can be argued that the time from the last experiment day would better describe the loss of trapped molecules, while isotope exchange probably occurs primarily after the samples are removed and exposed to an uncontrolled atmosphere. The relevance of de-trapping occurring over time depends on the fraction of H and D that is trapped as H_2, HD or D_2 compared to the fraction that is bound in various C_xH_y molecules. The nature of chemical bonds likely also affects the rate of isotope exchange, but the present measurements do not provide information for a detailed assessment.

The two data separation methods shown in Fig. 10, which are based on stopping power and full energy respectively, are fundamentally different from each other in the sense that the former distinguishes between different atomic numbers while the latter distinguishes between

different masses. These are both useful, and can be applied consecutively for improved separation in difficult cases, for example when treating samples containing ^{14}N, ^{15}N, ^{16}O, ^{18}O, ^{19}F and ^{20}Ne simultaneously. Such samples can be encountered in fusion applications in the case of tracer experiments combined with heavy metal hexafluoride puffing (WF_6, MoF_6), see for example Ref. [25]. In the present case, the B signal is not easily detected in the full energy plot (Fig. 10 b), as counts from ^{10}B are obscured by the high energy tail of the ^{9}Be signal, and ^{11}B by the low energy tail of ^{12}C. The stopping power plot (Fig. 10 a) remedies the problem. Ar, however, is better resolved in the full energy plot. Its stopping power is high enough that the full energy signal is almost reproduced also in Fig. 10 a. In this case, counts that are seen to belong to at least three distinct mass regions in Fig. 10 b all end up in one cluster marked "Ar" in Fig. 10 a. Counts in the two out of these three mass regions that are not Ar may come from Cl and Ca contamination from sample handling. Na contamination is further seen between the Ne and Si/P signals. There may be counts from K overlapping with Ar due to their similar mass, which is another reason for not reporting any numbers for the Ar concentration in this work.

5. Summary and concluding remarks

Deposits on SB and QMB covers retrieved from remote corners in the JET-ILW divertor have been studied with IBA, SEM and EDS. Layer thicknesses on the order of 1 μm or more were found on the plasma facing side of SB6 from ILW-1, while all other layers on SB were limited to less than 1 μm. Typical layer thicknesses 90° from the plasma facing direction on the SB were a few hundred nm, with slightly thicker layers on SB8-9 from ILW-3 than on SB4-6 from ILW-1, due to the longer divertor plasma time in ILW-3. The thickest deposit on the QMB covers from ILW-3, of $(5\pm2)\times10^{18}$ at/cm^2 or roughly 400 nm was found on QMB5 from the outer divertor. When it comes to the QMB covers from ILW-1-2, a C structure thicker than 1 μm was found on QMB5 from the outer divertor. Apart from this structure, the thickest layer was slightly less than $(3\pm1)\times10^{18}$ at/cm^2, on QMB2 from the inner divertor.

The main components of the deposits on QMB covers were Be and O, while a significant fraction of C was also present on the SB. The latter were mounted directly on the carbon ribs of the divertor carrier. This indicates a local transport of C from the divertor ribs to the spatial blocks, but not to the QMB covers, i.e. over a distance limited to a few cm. On all SB, as well as the QMB covers from ILW-1-2, Be and O occurred in similar concentrations possibly indicating the formation of BeO. Large areal densities of D were found in the C rich layers on the SB, and the D content seemed to scale with the total amount of C, rather than the layer thickness (see especially Tables 1 and 2). This is indicative of C/D co-deposition. As stated in Section 3.4, however, high atomic fractions of D were also found in the Be-rich layers with less C and O on QMB covers from ILW-3. We conclude therefore that the presence of C is not essential for D retention. The possibility of beryllium deuteride or deuteroxide formation has been treated in Ref. [26] and [27].

^{14}N was found throughout all analysed layers, at a level typically below or around 10 at.%. Ne and Ar were indicated in small amounts on QMB covers from ILW-1-2. The presence of these elements is not surprising, as they have been used for plasma edge cooling and disruption mitigation by massive gas injection. The detection of ^{18}O after its injection at the end of ILW-3 constitutes conclusive evidence for in-vessel oxidation of component surfaces.

Only a relatively small fraction of W, up to a few at.%, was present on SB after ILW-1. After ILW-3 a larger fraction was found, with almost 10 at.% of W close to the surface of SB8-9. The reason is likely that the strike point on the divertor tiles was closer to the corners in ILW-2-3 as compared to ILW-1, providing a local W source. The concentrations of Fe, Ni and Cr were low, less than or around 1 at.% at the surfaces of all deposits thick enough to completely cover the surface, but increasing close to the layer-substrate interface. In some points the concentrations reach around 5 at.% also further from the interface, as seen for Ni in Fig. 4 a.

High resolution microscopy revealed partially peeled off stratified structures as a possible dust source. The number of sublayers may be larger than what is observed with SEM here. See for example Ref. [28] and [29] where many sublayers are detected in stratified deposits on metallic mirrors and wall tiles from JET after analysis of the cross section by cutting with a focused ion beam. W, Mo and Cu particles with sizes less than or around 1 μm were found, the latter of which likely originated from the NBI system in JET's Octant 4. Module 14 IW in which the SB were mounted is located nearby in Octant 5.

Acknowledgments
This work has been carried out within the framework of the EUROfusion Consortium and has received funding from the Euratom research and training programme 2014-2018 under grant agreement number 633053. The views and opinions expressed herein do not necessarily reflect those of the European Commission. Work was performed under work package WPJET2. The Tandem Laboratory has been supported by grants from the Swedish Foundation for Strategic Research (SSF), grant number RIF14-0053, and the Swedish Council for Research Infrastructures (VR-RFI), grant number 821-2012-5144. Further support from the Swedish Research Council (VR), grant numbers 2015-04884 and 2017-00643 is gratefully acknowledged.

Data availability
The raw and processed data required to reproduce these findings are available to download from Mendeley Data via the links supplied with the online version of this paper.

References
[1] S. Brezinsek, J.W. Coenen, T. Schwarz-Selinger, K. Schmid, A. Kirschner, A. Hakola et al., Plasma-wall interaction studies within the EUROfusion consortium: progress on plasma-facing components development and qualification, Nucl. Fusion **57** (2017) 116041.

[2] G.F. Matthews, P. Edwards, T. Hirai, M. Kear, A. Lioure, P. Lomas et al., Overview of the ITER-like wall project, Phys. Scr. **T128** (2007) 137-143.

[3] V. Philipps, Ph. Mertens, G.F. Matthews, H. Maier and JET-EFDA contributors, Overview of the JET ITER-like Wall Project, Fusion Eng. Des. **85** (2010) 1581-1586.

[4] M. Rubel, J.P. Coad, A. Widdowson, G.F. Matthews, H.G. Esser, T.Hirai et al., Overview of erosion-deposition diagnostic tools for the ITER-Like Wall in the JET tokamak, J. Nucl. Mater. **438** (2013) S1204-S1207.

[5] H.G. Esser, V. Philipps, M. Freisinger, A. Widdowson, K. Heinola, A. Kirschner et al., Material deposition on inner divertor quartz-micro balances during ITER-like wall operation in JET, J. Nucl. Mater. **463** (2015) 796-699.

[6] G. Sergienko, H.G. Esser, A. Kirschner, A. Huber. M. Freisinger, S. Brezinsek et al., Quartz micro-balance results of pulse-resolved erosion/deposition in the JET-ILW divertor, Nucl. Mater. Energy **12** (2017) 478-482.

[7] J.P. Coad, H.-G. Esser, J. Likonen, M. Mayer, G. Neill, V. Philipps et al., Diagnostics for studying deposition and erosion processes in JET, Fusion Eng. Des. **74** (2005) 745-749.

[8] K. Heinola, A. Widdowson, J. Likonen, T. Ahlgren, E. Alves, C.F. Ayres et al., Experience on divertor fuel retention after two ITER-Like Wall campaigns, Phys. Scr. **T170** (2017) 014063.

[9] P. Ström, P. Petersson, M. Rubel, G. Possnert, A combined segmented anode gas ionization chamber and time-of-flight detector for heavy ion elastic recoil detection analysis, Rev. Sci. Instrum. **87** (2016) 103303.

[10] K. Arstila, J. Julin, M.I. Laitinen, J. Aalto, T. Konu, S. Kärkkäinen et. al., Potku – New analysis software for heavy ion elastic recoil detection analysis, Nucl. Instrum. Meth. **B331** (2014) 34-41.

[11] E. Morast, E. Svantesson, Efficiency of a Time-of-Flight Detection System for Analysis of Wall Material From Controlled Fusion Devices, Student thesis, KTH Royal Institute of Technology (2017), urn:nbn:se:kth:diva-214736.
Online: http://urn.kb.se/resolve?urn=urn:nbn:se:kth:diva-214736,
accessed 2018-05-04.

[12] M. Janson, CONTES: Conversion of Time-Energy Spectra, Users Manual (2004).

[13] M. Mayer, SIMNRA, a simulation program for the analysis of NRA, RBS and ERDA, AIP Conference Proceedings **475** (1999) 541-544.

[14] E.A. Wolicki, H.D. Holmgren, R.L. Johnston, E. Geer Illsley, Differential Cross Sections for the $Be^{9}(He^{3}, p)B^{11}$ Reaction, Phys. Rev. **116** (1959) 1585-1591.

[15] V. Kh. Alimov, M. Mayer, J. Roth, Differential cross-section of the $D(^{3}He,p)^{4}He$ nuclear reaction and depth profiling of deuterium up to large depths, Nucl. Instrum. Methods Phys. Res. **B234** (2005) 169-175.

[16] M.E. Adel, O. Amir, R. Kalish, L.C. Feldman, Ion-beam-induced hydrogen release from a-C:H: A bulk molecular recombination model, J. Appl. Phys. **66** (1989) 3248-3251.

[17] J. Roth, B.M.U. Scherzer, R.S. Blewer, D.K. Brice, S.T. Picraux, W.R. Wampler, Trapping, detrapping and replacement of keV hydrogen implanted into graphite, J. Nucl. Mater. **93-94** (1980) 601-607.

[18] M. Rubel, H. Bergsåker, P. Wienhold, Ion-induced release of deuterium from co-deposits by high energy helium bombardment, J. Nucl. Mater. **241-243** (1997) 1026-1030.

[19] H. Bergsåker, I. Bykov, P. Petersson, G. Possnert, J. Likonen, S. Koivuranta, J. P. Coad, A.M. Widdowson, JET EFDA contributors, Microstructure and inhomogeneous fuel trapping at divertor surfaces in the JET tokamak, Nucl. Instrum. Methods Phys. Res. **B332** (2014) 266-270.

[20] F. Schiettekatte, M. Chicoine, S. Gujrathi, P. Wei, K. Oxorn, Allegria: a new interface to the ERD program, Nucl. Instrum. Methods Phys. Res. **B219-220** (2004) 125-129.

[21] P. Ström, P. Petersson, M. Hamberg, Surface oxide and roughness on test samples for the Ultra High Vacuum section of the Laser Heater for the European XFEL, Vacuum **149** (2018) 83-86.

[22] J.F. Ziegler, M.D. Ziegler, J.P. Biersack, SRIM – The stopping and range of ions in matter (2010), Nucl. Instrum. Methods Phys. Res **B268** (2010) 1818-1823.

[23] M.J. Rubel, G. De Temmerman, G. Sergienko, P. Sundelin, B. Emmoth, V. Philipps, Fuel removal from plasma-facing components by oxidation-based techniques. An overview of surface conditions after oxidation, J. Nucl. Mater. **363-365** (2007) 877-881.

[24] W. Wang, W. Jacob, J. Roth, Oxidation and hydrogen isotope exchange in amorphous, deuterated carbon films, J. Nucl. Mater. **245** (1997) 66-71.

[25] P. Ström, P. Petersson, M. Rubel, A. Weckmann, S. Brezinsek, A. Kreter, S. Möller, K. Rozniatowski, Characterisation of surface layers formed on plasma-facing components in controlled fusion devices: Role of heavy ion elastic recoil detection, Vacuum **122** (2015) 260-267.

[26] R.P. Doerner, M.J. Baldwin, D. Buchenauer, G. De Temmerman, D. Nishijima, The role of beryllium deuteride in plasma-beryllium interactions, J. Nucl. Mater. **390-391** (2009) 681-684.

[27] C. Makepeace, C. Pardanaud, M. Kumar, C. Martin, Y. Ferro, E. Hodille et al., The effect of Beryllium Oxide on retention in JET ITER-like wall tiles, 23rd International Conference on Plasma Surface Interactions in Controlled Fusion Devices (2018).

[28] M. Rubel, S. Moon, P. Petersson, A. Garcia-Carrasco, A. Hallén, A. Krawczynska et al., Metallic mirrors for plasma diagnosis in current and future rectors: tests for ITER and DEMO, Phys. Scr. **T170** (2017) 014061.

[29] E. Fortuna-Zaleśna, J. Grzonka, M. Rubel, A. Garcia-Carrasco, A. Widdowson, A. Baron-Wiechec et al., Studies of dust from JET with the ITER-Like Wall: Composition and internal structure, Nucl. Mater. Energy **12** (2017) 582-587.